KeA1

CHINESE ROOTS
GLOBAL IMPACT

Contents lists available at ScienceDirect

Advanced Powder Materials

journal homepage: www.keaipublishing.com/en/journals/advanced-powder-materials



Revisiting catalytic performance of supported metal dimers for oxygen reduction reaction *via* magnetic coupling from first principles



Linke Yu^a, Fengyu Li^{a,*}, Jingxiang Zhao^{b,**}, Zhongfang Chen^{c,***}

- ^a School of Physical Science and Technology, Inner Mongolia University, Hohhot, 010021, China
- b College of Chemistry and Chemical Engineering, Key Laboratory of Photonic and Electronic Bandgap Materials, Ministry of Education, Harbin Normal University, Harbin, 150025. China
- ^c Department of Chemistry, University of Puerto Rico, Rio Piedras Campus, San Juan, PR, 00931, USA

ARTICLE INFO

Keywords: First-principles calculations Double-atom catalysts Oxygen reduction reaction Magnetic coupling d-band center

ABSTRACT

In this study, we selected 10 Co-based double-atom catalysts (DACs) catalysts, namely $CoMN_6$ -gra(OH) (M = Sc, Ti, V, Cr, Mn, Fe, Co, Ni, Cu, Zn), and investigated their oxygen reduction reactions (ORR) catalytic performances with/without considering the magnetic coupling by means of density functional theory (DFT) calculations. It was found that $CoNiN_6$ -gra(OH), $CoCuN_6$ -gra(OH), and $CoZnN_6$ -gra(OH) exhibit good catalytic activity of ORR (with low overpotentials of 0.33, 0.34 and 0.23 V, respectively) when the magnetic coupling is considered. In particular, magnetic changes in $CoMN_6$ -gra(OH) candidates play a vital role in their ORR catalytic activity. Interestingly, the d-band center can be utilized to well rationalize the ORR catalytic activity. This work highlights the importance of considering the magnetic coupling to well predict the activity of ORR catalysts, and discloses that the manipulation of the magnetic coupling between transition metal atoms is an emerging and powerful approach for the development of high-performance electrocatalysts for ORR and other related reactions.

1. Introduction

Because of the growing energy consumption, climate change, and environmental and ecological effects of greenhouse gas emissions, great efforts have been made to develop renewable and sustainable energies to replace the fossil fuels [1-3]. Fuel cells, as energy conversion devices, have high conversion efficiency, low pollutant emission, and low energy waste, among which the proton exchange membrane fuel cells (PEMFC) deliver high power density and have the advantages of low noise, wide range of applications, and low operating temperature compared with other fuel cells [4-10]. However, the slow oxygen reduction reaction (ORR) of the cathode is one key factor restraining the efficiency of energy conversion [11,12], and catalysts with high ORR activity are of a great need [13,14]. Currently, Pt and its alloys are the most common and efficient electrocatalysts, however, their high cost, scarce earth reserves, and poor long-term stability pose a major obstacle to their wide applications [15–19]. Therefore, it is critical to develop low-cost alternatives with high ORR catalytic efficiency.

To date, a variety of ORR catalysts with promise to replace Pt and its

alloys have been reported, such as metal-free heteroatom-doped graphenes [20-22], black phosphorus [23,24], nanowires [25,26], transition metal oxides and nitride [27,28], metal clusters [29-31], and composites [32,33]. Single-atom catalysts (SACs), in which individual atoms are well dispersed on the support, have shown remarkable performance as ORR catalysts [34-41]. The great success of SACs have also inspired the development of double-atom catalysts (DACs), in which metal dimers are anchored on supporting substrate materials [42-44]. Notably, recent experimental and theoretical studies have shown that the introduction of a second metal atom can change the electronic properties of the catalyst and further improve the ORR activity [45-56]. For example, Xiao et al. synthesized binuclear Co2N5 sites, which have much higher ORR activity than the single CoN₄ active site [45]. The binuclear Fe-Ni [46] and Co-Ni [48] embedded in N-doped carbon were observed to possess outstanding catalytic performance in oxygen reduction and evolution reactions. The Co-Zn catalyst was reported to exhibit excellent ORR performance under both alkaline and acidic conditions [49]. On the other hand, by means of density functional theory (DFT) computations, Xia and coworkers designed new dispersed metal-atom catalysts with

E-mail addresses: fengyuli@imu.edu.cn (F. Li), xjz_hmily@163.com (J. Zhao), zhongfang.chen1@upr.edu (Z. Chen).

^{*} Corresponding author.

^{**} Corresponding author.

^{***} Corresponding author.

single-, dual-, and tri-metallic sites, and found that a variety of catalysts in dual-sites with metal bonds have excellent ORR performance [50]. Quite recently, by DFT computations, Deng et al. investigated the catalytic performance towards ORR of over 80 homo- or hetero-nuclear DACs with N-doped graphene as the support, and their machine learning studies showed that their activity was mainly governed by simple geometric parameters [51].

Identifying the key factors and appropriate approaches to improve the catalytic efficiency of ORR catalysts will greatly facilitate the computational screening and design of these catalysts [57-59]. One important factor is the coordination environment of the active site. For example, Zhang et al. identified the CoN₄-gra as the best bifunctional catalyst among the Co and N codoped graphene SACs (CoN_x-gra, x = 1–4) [60]. Ligand substitution [61,62] and modification of the first and second coordination spheres [63] have also been confirmed to be effective. Very recently, it was proposed that the spin state of single transition metal atom associates with chemical adsorption of reaction intermediates and the reaction pathways, and tuning the spin state of active site is an emerging strategy to improve the catalytic activity of SACs. For instance, in 2018, Jiang and coworkers found that the adsorbed CO molecule not only changes the spin of the active site of FeN₃ embedded on graphene, but also affects the spin of the adjacent site, and called for attention to the cooperative spin transition between adjacent active sites on SACs [64]. In 2020, they demonstrated that manipulating the spin state of single Co atom in covalent organic frameworks can improve the photocatalytic performance [65]. In 2021, they proposed using electronic spin moment as a catalytic descriptor for the ORR activity of Fe SACs supported on C2N monolayer [66], and showed that controlling the spin state of MoS₂ by adopting suitable doped metal atoms or their adsorption sites can achieve improved NRR catalytic activity [67]. However, the effect of spin states in DACs, especially the magnetic coupling between the two metal atoms, have not received much attention.

In this work, we aimed to find out whether the magnetic coupling of DACs could improve the catalytic efficiency for ORR by means of DFT computations. Considering that DACs with the participation of Co usually have good catalytic performance for ORR [49-51], we combined Co and 3d transition metals as the dual-metal sites in N-doped graphene (CoMN₆-gra, M = Sc, Ti, V, Cr, Mn, Fe, Co, Ni, Cu, Zn, Fig. 1a), and investigated their catalytic performance for ORR. Note that such configurations have been widely adopted in previous theoretical studies [51, 68] and have also been synthesized experimentally [69]. By comparing the energies of nonmagnetic, ferromagnetic (Fig. 1b), and antiferromagnetic (Fig. 1c) orderings in each elementary step during the ORR process, we found that the ORR efficiency can be improved when the magnetic coupling is considered. This work underlines the importance of spin states in designing DACs for ORR and related electrochemical processes, and demonstrates that tuning the magnetic coupling between transition metal atoms is a powerful but nearly neglected approach to improve the catalytic activity of electrocatalysts.

2. Computational methods

For systems without strong spin-orbital coupling (SOC), typically we can predict the properties of materials without magnetic properties using the spin-unpolarized DFT computations, and predict the properties of magnetic materials by the spin-polarized DFT. Since the chemical reactions involve bond stretching, breaking, and formation, and radicals are common intermediates, the spin-unpolarized DFT is not an option for studying the catalytic process, while the spin-polarized DFT is of a good choice.

Nevertheless, for nonmagnetic (NM) materials, the spin-polarized DFT computations will give the same result as the spin-unpolarized DFT computations: during the minimization process, the spin-density "dependent" exchange functional will converge to the spin-density "independent" exchange functional. When studying magnetic materials with the spin-polarized DFT and the default setting in VASP, typically, a

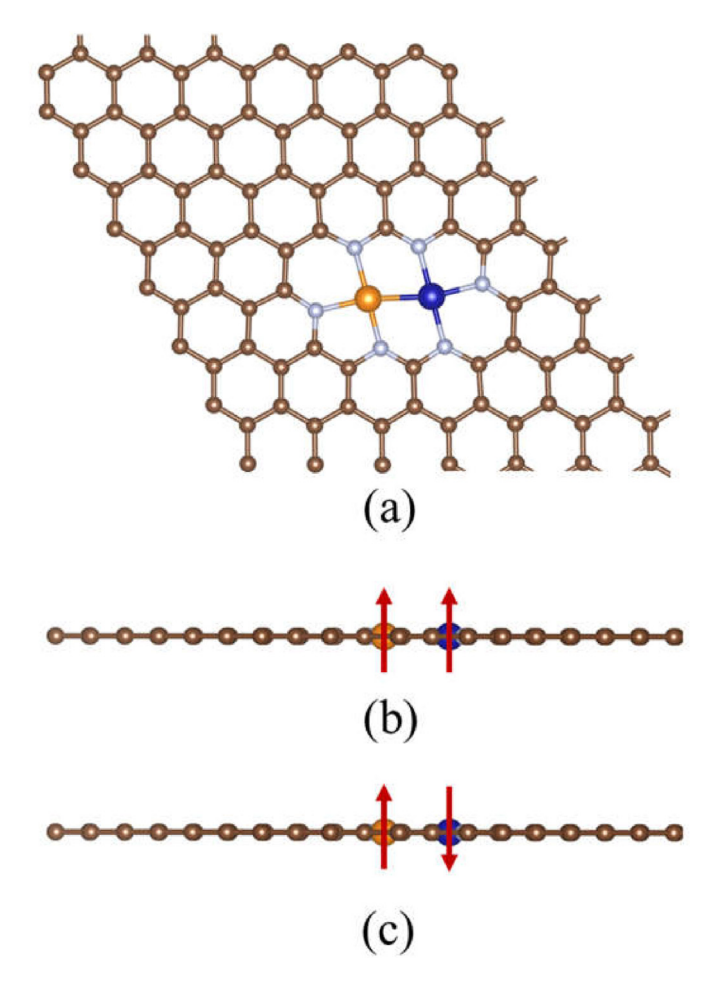


Fig. 1. (a) Structural illustration of CoMN₆-gra model. (b,c) Schematic diagrams of ferromagnetic and antiferromagnetic orderings. Color scheme: C, brown; N, silver; Co, blue; M, yellow.

ferromagnetic (FM) state is obtained, which is exemplified by ${\rm CoZnN_{6}}$ gra(OH) in this work: the spin-polarized DFT with the default setting of magnetic order revealed that each key intermediate during the ORR process is ferromagnetic, as shown in Table S1. However, using such a default setting, the lower-energy antiferromagnetic (AFM) ground state is not located.

Consequently, the magnetic coupling between the two metal atoms in DACs, *i.e.*, the preference of adopting anti-ferromagnetic group state for some reaction steps in the electrochemical process, might escape the attention. For example, many open-shell transition metal (TM) atoms possess certain magnetic moments, whereas only a few of them (like Fe, Co, Ni) exhibit ferromagnetism in their crystalline state. Moreover, the combination of different types and number of atoms would lead to tunable magnetism in the alloy clusters, even beyond the current magnetic alloy of solid phase [70].

DFT computations were performed using the Vienna *Ab initio* Simulation Package (VASP) [71,72]. The spin-polarized calculations were carried out unless mentioned otherwise. The interactions between ion cores and valence electrons were described by the projector augmented wave (PAW) method [73]. The Perdew-Burke-Ernzerhof (PBE) functional was used to describe the exchange-correlation energy [74]. The energy cutoff was chosen as 500 eV [75]. The Monkhorst-Pack (MP) scheme of 3 \times 3 \times 1 k-points was adopted to sample the Brillouin zone. The van der Waals (vdW) interactions between the reactants/intermediates and the catalyst were considered using the DFT-D2 method [76]. For 3d transition metals (M), DFT + U (U = 4 eV) method was also considered in the calculations [77]. Note that the U values may have influence on the

energy and magnetism, so we tested different U values for $CoNiN_6@gra$, and our results showed that the relative energies and magnetism of each magnetic state do depend on the U values (Table S2). However, all the four considered U values (U=3, 4, 5 and 6 eV) locate the AFM as the energy-preferred state, and the magnetic moment on Co/Ni atom yielded at U=4 eV is acceptably close to U=6 eV (-1.98 vs -2.53/0.52 vs 0.77 μ_B). We therefore used the uniform U (4 eV) for all transition metal elements in our study. The convergence criterion for the energy of self-consistent iteration is 1×10^{-6} eV, and that for the force is 0.02 eV/Å on each atom. The Poisson-Boltzmann implicit solvation model with a dielectric constant of $\varepsilon=80$ for water was used to simulate the H_2O solvent environment [78].

As shown in Fig. 1, we used a 7×7 supercell of graphene in the calculations. To avoid the interaction between two neighboring surfaces, a vacuum space $\sim 20 \text{ Å}$ was applied [79,80].

The overall reaction of ORR is

$$O_2(g) + 4H^+ + 4e^- \rightarrow H_2O(l)$$
 (1)

The four elementary reaction steps during ORR in acidic media are as follows:

$$O_2(g) + H^+ + e^- + * \rightarrow *OOH$$
 (2)

*OOH + H⁺ + e⁻
$$\rightarrow$$
 *O + H₂O(l) (3)

$$*O + H^{+} + e^{-} \rightarrow *OH$$
 (4)

*OH + H⁺ + e⁻
$$\rightarrow$$
 H₂O(l) + *

where "*" denotes the adsorption site. The absorbed energy is calculated by Refs. [81,82]:

$$\Delta E_{*O} = E(*O) - E(*) - (E_{H_2O} - E_{H_2})$$
(6)

$$\Delta E_{^{*}OH} = E(^{*}OH) - E(^{*}) - \left(E_{H_{2}O} - \frac{1}{2}E_{H_{2}}\right)$$
 (7)

$$\Delta E_{*OOH} = E(*OOH) - E(*) - \left(2E_{H_2O} - \frac{3}{2}E_{H_2}\right)$$
 (8)

where E(*) is the ground state energy of catalyst; $\Delta E_{^{*}\mathrm{O}}$, $\Delta E_{^{*}\mathrm{OH}}$, and $\Delta E_{^{*}\mathrm{OOH}}$ are the ground state energies of O, OH, and OOH adsorbed catalysts, respectively; $E_{\mathrm{H_2O}}$ and $E_{\mathrm{H_2}}$ are the energies of water and hydrogen molecules of gas phase in a cube of 20 Å × 20 Å, respectively.

The free energy of a reaction step is calculated by the following equation:

$$\Delta G = \Delta E_{\rm DFT} + \Delta ZPE - T\Delta S + \Delta G_{U_0} - \Delta G_{\rm pH}$$
 (9)

where ΔE_{DFT} is the reaction energy obtained from the DFT calculations directly; ΔZPE and $T\Delta S$ are the contributions of the zero-point energy (ZPE) and entropy, respectively [83]; the pH related term ΔG_{pH} is determined by $\Delta G_{\mathrm{pH}} = k_{\mathrm{B}}T \times \ln 10 \times \mathrm{pH}$, of which k_{B} is the Boltzmann constant, and pH is set as 0 in our work, thus $\Delta G_{\mathrm{pH}} = 0$; U_0 is the potential with respect to the standard hydrogen electrode (SHE) at standard conditions ($U_0 = 0$ V, $\mathrm{pH} = 0$, $\mathrm{p} = 1$ bar, T = 298.15 K). The free energy of a free O_2 is determined by the following equation in our study [84]:

$$G_{\rm O_2} = 2G_{\rm H_2O} - 2G_{\rm H_2} + 4.92 \tag{10}$$

where $G_{\rm H_2O}$ and $G_{\rm H_2}$ are the free energies of $\rm H_2$ and $\rm H_2O$ molecule.

The $\Delta G_1 - \Delta G_4$ of each step of the ORR can be obtained by the following expressions:

$$\Delta G_1 = \Delta G_{^{*}\text{OOH}} - 4.92 \text{ eV}$$
 (11)

$$\Delta G_2 = \Delta G_{*0} - \Delta G_{*00H} \tag{12}$$

$$\Delta G_3 = \Delta G_{^*\text{OH}} - \Delta G_{^*\text{O}} \tag{13}$$

$$\Delta G_4 = -\Delta G_{^{*}\text{OH}} \tag{14}$$

The limiting potential (U_L), which is also called the working potential, is used to evaluate the catalytic performance [85–88]. Here, U_L represents the maximum free energy change in Eqs. (11)-(14) and is expressed as Eq. (15):

$$U_{\rm L} = -\frac{\max(\Delta G_1, \Delta G_2, \Delta G_3, \Delta G_4)}{\rho} \tag{15}$$

The overpotential (η_{ORR}) of the whole ORR (in the unit of eV) can be obtained following Eq. (16):

$$\eta_{\text{ORR}} = 1.23 - U_{\text{L}} = 1.23 + \frac{\max(\Delta G_1, \Delta G_2, \Delta G_3, \Delta G_4)}{e}$$
(16)

3. Results and discussion

3.1. Stability of DACs

The stability of the DACs in our work was evaluated by calculating the binding energy of the anchored metal dimer (Co and M) on graphene as follows:

$$E_{\rm b} = \frac{1}{2} \left(E_{\rm CoMN_6-gra} - E_{\rm N_6-gra} - E_{\rm Co} - E_{\rm M} \right)$$
 (17)

where $E_{\text{CoMN}_6-\text{gra}}$ and $E_{\text{N}_6-\text{gra}}$ are the energies of nitrogen-doped graphene with and without adsorbing transition metal atoms, respectively, E_{Co} and E_{M} are the energies of a single Co and M atom, respectively. Then, the binding energy was compared with the average cohesion energy (E_{coh}) of transition metal atoms in bulk phase by the equation $\Delta E = E_{\text{b}} - E_{\text{coh}}$ [79], where the average cohesion energy is determined by Eq. (18):

$$E_{\rm coh} = \frac{1}{2} (E_{\rm coh-Co} + E_{\rm coh-M}) \tag{18}$$

where $E_{\mathrm{coh-Co}}$ and $E_{\mathrm{coh-M}}$ are the cohesive energies of Co and M metals, respectively. As shown in Table S3, the binding strength of metal dimers on N₆-gra support are all stronger than the average cohesive energies of metal bulk, suggesting the good stability of these DACs. The distances between Co and M in all CoMN₆-gra configurations (Table S3) increase gradually as the number of electrons outside the nucleus of element M increases.

The magnetic properties of the ten $CoMN_6$ -gra catalysts are also given in Table S3. $CoScN_6$ -gra, $CoVN_6$ -gra, $CoCoN_6$ -gra and $CoCuN_6$ -gra exhibit ferromagnetic properties, and the remaining six catalysts ($CoTiN_6$ -gra, $CoCrN_6$ -gra, $CoMnN_6$ -gra, $CoFeN_6$ -gra, $CoMiN_6$ -gra and $CoZnN_6$ -gra) are antiferromagnetic. When using the default settings in the spin-polarized calculations, only two DACs ($CoMnN_6$ -gra and $CoFeN_6$ -gra) were predicted in the antiferromagnetic ground-state, while the remaining eight catalysts all are ferromagnetic, particularly, the antiferromagnetic order of $CoTiN_6$ -gra, $CoCrN_6$ -gra, $CoNiN_6$ -gra and $CoZnN_6$ -gra was failed to be located ($CoMnN_6$ -gra, $CoMiN_6$ -gra and $CoMiN_6$ -gra was failed to be located ($CoMiN_6$ -gra). Therefore, quite different magnetic order was predicted by spin-polarized DFT computations when using default setting or well considering the magnetic coupling.

To verify that the 7×7 supercell (the lateral dimension is $\sim\!17.16$ Å) is large enough, we evaluated the magnetic properties of a 14×7 supercell for $CoCoN_6$ -gra. The relative energies of nonmagnetic, ferromagnetic and antiferromagnetic orderings agree well with those of a 7×7 supercell (Table S4), confirming that a 7×7 supercell is large enough to avoid image interactions.

Since OH species have strong binding at the CoMN₆-gra active site, and the previous studies showed that the adsorbed OH species would

enhance the ORR activity [50,51,89–91], we adopted structures with pre-adsorbed *OH species at the active center as our DAC models, referred as $CoMN_6$ -gra(OH), to explore their O_2 adsorption and ORR performance (Fig. 2). Notably, four (out of 10) DACs examined in this work, namely, $CoScN_6$ -gra(OH), $CoVN_6$ -gra(OH), $CoVN_6$ -gra(OH), adopt the generally ignored AFM state as the ground state (Table 1), and among them, both $CoScN_6$ -gra(OH) and $CoVN_6$ -gra(OH) take the AFM state instead of the FM state adopted by their *OH-free counterparts, indicating that the intermediate adsorption is vital to regulate the magnetic configuration of the metal dimers.

Note that the adsorbates may alter the easy axis (EA) and the magnetic anisotropy energy (MAE) for the ferromagnetic systems [92]. We examined the EA and MAE for ferromagnetic CoCuN $_6$ -gra and CoCuN $_6$ -gra(OH). Our results revealed that the adsorption of OH will not alter the EA (both are along *y*-axis direction), and the MAE is increased from 0.21 to 1.36 meV when OH is adsorbed (Table S5). However, such small variation is negligible for the free energy change and the limiting potential prediction.

3.2. Adsorption of O2

The O_2 adsorption is the precondition for the ORR. Thus, we first examined the adsorption of O_2 on these DACs. The O_2 molecule prefers to be adsorbed over the Co-M bridge site with the end-on configuration (Fig. S1). We selected the lowest energy state of the magnetic configuration as the magnetic ground state, and calculated the free energy of O_2 adsorption (Table S6). Interestingly, except for CoCrN₆-gra(OH) and CoMnN₆-gra(OH) which preserves the AFM character, the adsorption of O_2 changed the magnetic coupling between Co and M of all the other DACs. The FM state of CoTiN₆-gra(OH), CoFeN₆-gra(OH), CoNiN₆-gra(OH) and CoCuN₆-gra(OH) was switched to AFM upon O_2 adsorption, the AFM state of CoScN₆-gra(OH) and CoVN₆-gra(OH) was changed to FM, and the NM state of CoZnN₆-gra(OH) and CoCoN₆-gra(OH) was

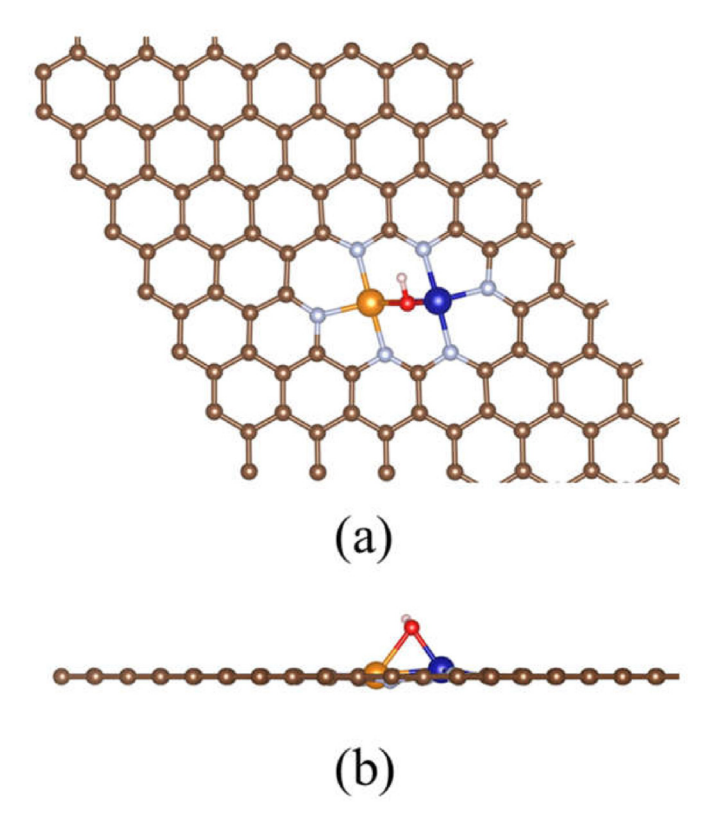


Fig. 2. Model of $CoMN_6$ -gra with pre-sorption of OH species, top view (a) and side view (b). Color scheme: C, brown; N, silver; Co, blue; M, yellow; O, red; H, pink.

Table 1
Relative energies of NM, FM and AFM states of examined DACs with adsorbed *OH species, where the lowest energy state was set as zero (eV).

catalysts	NM	FM	AFM
CoSc(OH)	0.04	0.01	0.00
CoTi(OH)	0.17	0.00	0.01
CoV(OH)	0.46	0.56	0.00
CoCr(OH)	2.39	0.02	0.00
CoMn(OH)	2.27	0.23	0.00
CoFe(OH)	0.92	0.00	0.18
CoCo(OH)	0.00	0.00	0.01
CoNi(OH)	0.50	0.00	0.49
CoCu(OH)	0.71	0.00	0.01
CoZn(OH)	0.00	0.00	0.00

modulated to FM and AFM, respectively (Table S7). For all these catalysts, the length of the O—O bond of the adsorbed O $_2$ (1.30–1.33 Å) was elongated by \sim 0.1 Å compared to the length of free molecule (1.21 Å), and 0.52–0.81 electrons were transferred from the DACs to the O $_2$ according to Bader charge analysis (Table S6), indicating that the adsorbed * O $_2$ is activated.

3.3. Catalytic performance of DACs with/without well considering magnetic coupling

In order to unveil the effect of magnetic coupling on the catalytic performance of the CoMN₆-gra(OH), we first computed the free energy changes of the key reaction steps. For each intermediate adsorbed DACs, a few possible configurations were examined and the lowest-energy ones were chosen. Both ferromagnetic (FM) and antiferromagnetic (AFM) coupling between Co and M atoms as well as the nonmagnetic (NM) state were considered for the 10 CoMN₆-gra(OH) DACs. Note that the spin-unpolarized computations were also performed for the cases in which the NM state was not located in the spin-polarized computations to obtain the NM state for comparison. The relative energies of the three states with respect to the ground state for each ORR intermediate were compared in Table S7.

We found that the magnetic orderings of the 10 examined DACs change during the ORR process (Fig. 3 and Fig. S2). For example, the *O2-adsorbed CoNiN₆-gra(OH) alters from antiferromagnetism to nonmagnetic when *O2 is reduced to *OOH, and CoNiN₆-gra(OH) switches back to ferromagnetic coupling upon *O and *OH adsorption, i.e., during the whole ORR process * \rightarrow *O2 \rightarrow *OOH \rightarrow *O \rightarrow *OH \rightarrow * + H2O, the magnetic coupling of CoNiN₆-gra(OH) is FM \rightarrow AFM \rightarrow NM \rightarrow FM. For the case of CoCuN₆-gra(OH), the magnetic variation is FM \rightarrow AFM \rightarrow NM \rightarrow AFM \rightarrow NM \rightarrow FM, while for CoZnN₆-gra(OH), when considering magnetic coupling, the magnetic change in the reaction steps is NM \rightarrow FM \rightarrow FM \rightarrow FM \rightarrow NM \rightarrow NM.

When involving the magnetic coupling, we calculated the free energy change of each elementary step, the limiting potential, and the overpotential (η_{ORR}), and the results are summarized in Table S8. Note that the obtained η_{ORR} order, CoZn (0.23 V) < CoNi (0.33 V) < CoCu (0.34 V) < CoCo (0.58 V) < CoMn (0.88 V) < CoFe (1.02 V) < CoCr (1.42 V) <CoV (1.95 V) < CoSc (2.01 V) < CoTi (2.40 V), is quite different to the sequence obtained by Deng et al. [51], CoNi (0.35 V) < CoCo (0.41 V) < CoZn (0.43 V) < CoCu (0.45 V) < CoMn (0.91 V) < CoFe (1.00 V), forwhich the computations were carried out by setting the magnetic configuration as default values (but not essentially in the magnetic ground state). Actually, we computed the overpotential for CoZnN₆-gra(OH) with the magnetic configuration set as default value, and our results agreed well with Deng et al.'s [51]: the same potential-determining step (PDS) (*OH \rightarrow H₂O(l)) and very close η_{ORR} values (0.39 vs 0.43~V, the slight difference might be assigned to the different methods of dispersion correction) (Table S9). Thus, we took their results as an example for the simulations, in which the magnetic configuration is set as default values.

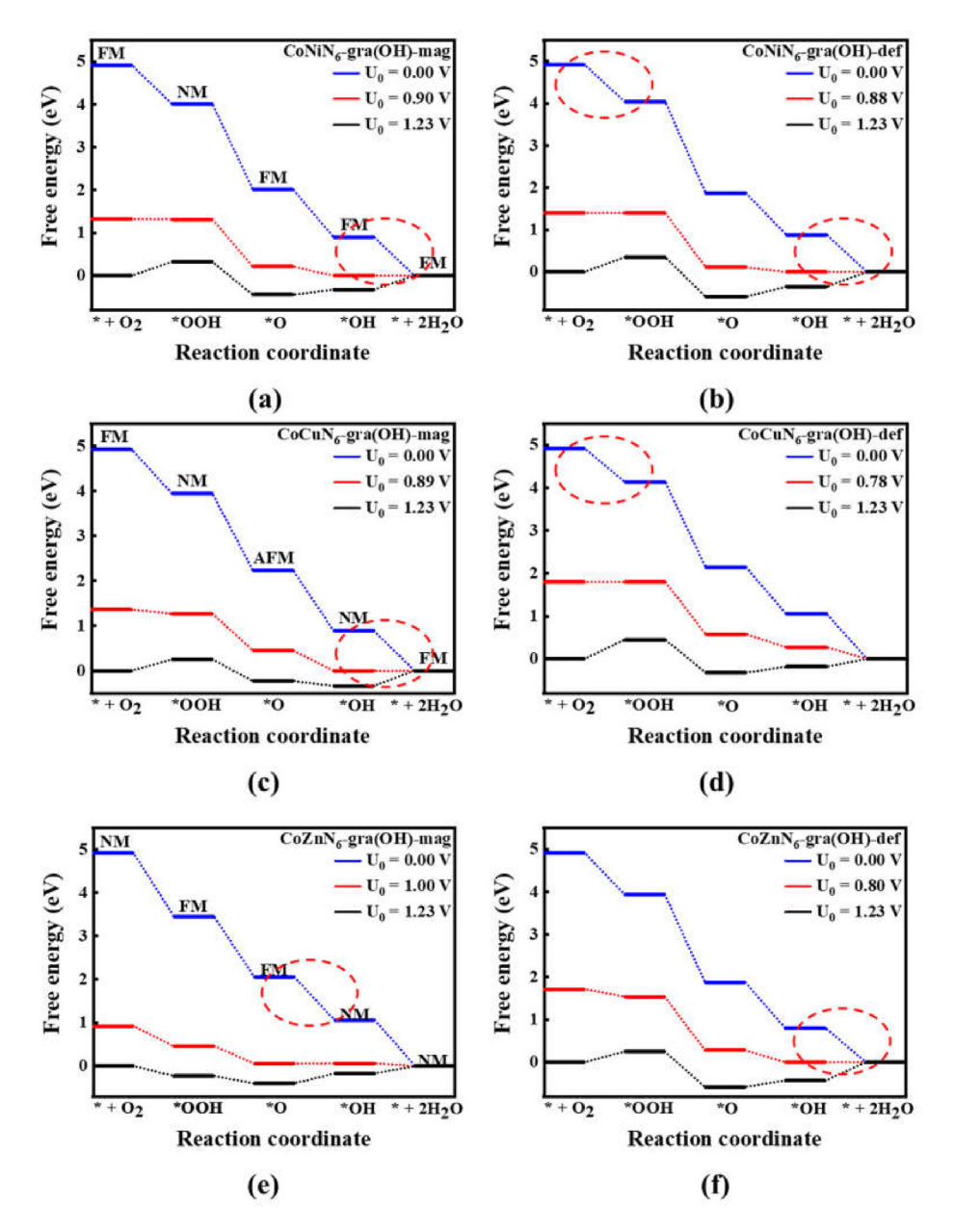


Fig. 3. Free energy diagrams of ORR over three DACs with considering magnetic coupling (left panel) and with magnetic configuration set as default value (right panel, results from the article by Deng et al. [51]) for CoNiN₆-gra(OH) (a and b), CoCuN₆-gra(OH) (c and d), and CoZnN₆-gra(OH) (e and f) at $U_0 = 0$ V (blue), $U_0 = U_L$ (red), and $U_0 = 1.23$ V (black). '*r' represents the adsorption site. The potential-determining step was highlighted by dashed ellipse.

We carefully examined the calculated limiting potentials (Fig. 3 and Fig. S2) by the spin-polarized DFT computations when the magnetic coupling was considered and when it was not well addressed (with the magnetic configuration set as default value). When the magnetic coupling was considered, three catalysts, CoMN₆-gra(OH) (M = Ni, Cu, Zn), stand out among the 10 DACs since their limiting potentials are about 1 V (0.90, 0.89 and 1.00 V, respectively; Fig. 3). The geometric configurations and the spatial spin density distributions of the ORR intermediates adsorbed on these three DACs are presented in Fig. 4, in which the AFM ground state of *O–CoCuN₆-gra(OH) is clearly shown by the magnetic distribution. Moreover, the calculated ORR overpotential when considering the magnetic coupling is generally lower, since the intermediates involved in the potential-determining step are of lower energies under such a treatment.

Well treating the magnetic coupling or not may give different PDS. Though in both cases the same PDS (the reduction of *OH) can be obtained for $CoNiN_6$ -gra(OH), different results arise for $CoCuN_6$ -gra(OH)

and $CoZnN_6$ -gra(OH). When clearly including the magnetic coupling, the formation of *OOH and the reduction of *OH are the PDS for ORR on $CoCuN_6$ -gra(OH) and $CoZnN_6$ -gra(OH), respectively; while when the magnetic coupling is not well considered, the reduction of *OH and the reduction of *O are predicted as the PDS on these two catalysts (Table S10).

Among all the examined catalysts, CoZnN₆-gra(OH) has the highest limiting potential, thus deserving further explorations. When the magnetic coupling is considered (Fig. 3e), the free energy changes for the four elementary steps are $-1.46,\,-1.40,\,-1.00$ and -1.06 eV, respectively, all approaching to the optimal value of -1.23 eV, resulting in an overpotential (η_{ORR}) of 0.23 V, and the corresponding PDS is *O (FM) \rightarrow *OH (NM). For comparison, we also evaluated the ORR performance of CoZnN₆-gra(OH) in the nonmagnetic case using the spin-unpolarized DFT computations. The calculated η_{ORR} value is 0.38 V, quite close to 0.39 V obtained when setting the magnetic configuration as default value (Table S9). However, the predicted PDS is the *OOH generation (O₂(g) \rightarrow

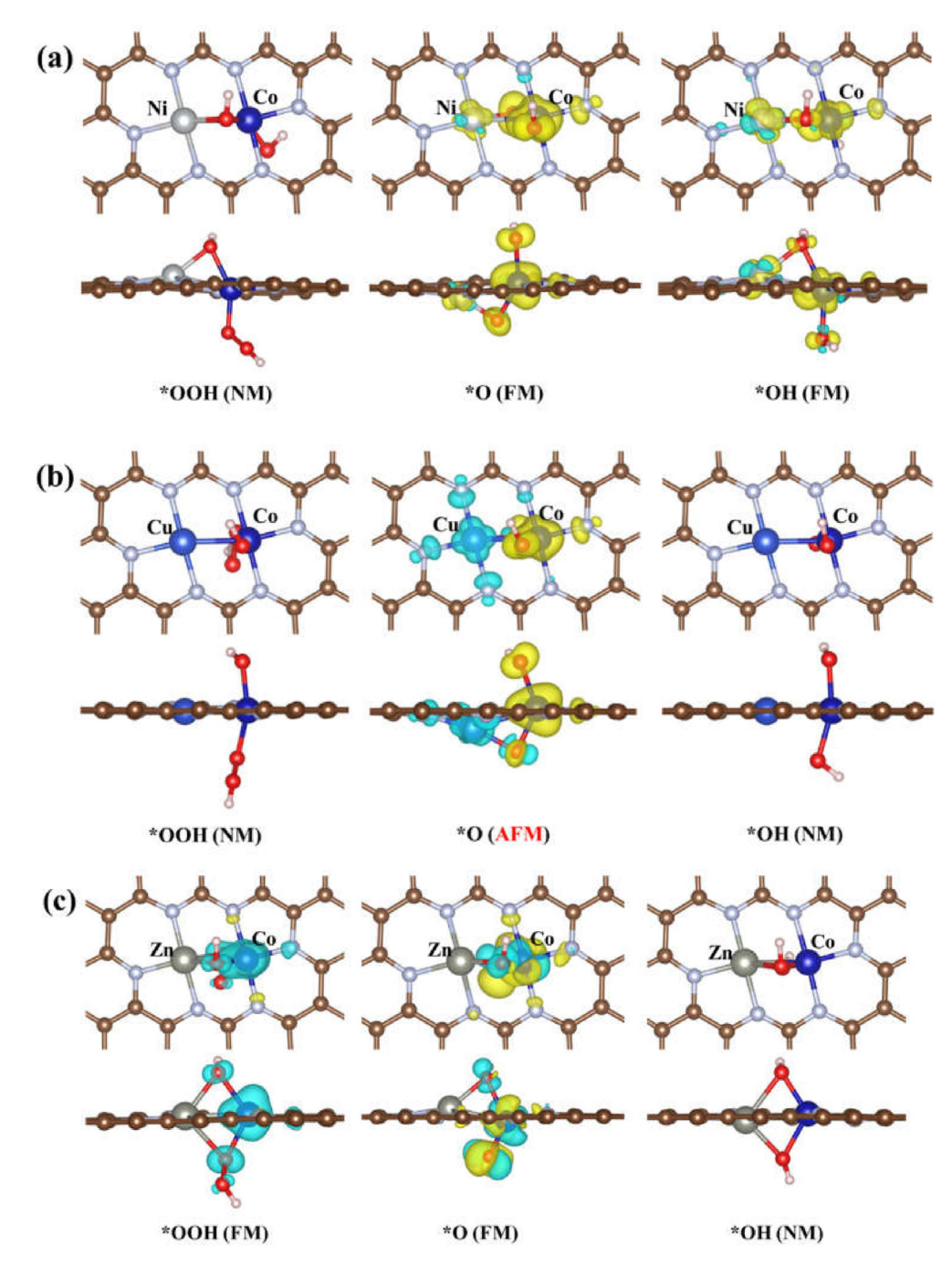


Fig. 4. Spatial spin density distributions of CoNiN₆-gra(OH) (a), CoCuN₆-gra(OH) (b) and CoZnN₆-gra(OH) (c) with adsorption of *O, *OH and *OOH species, respectively (Isosurface value = 0.0055 e/Å^3).

*OOH) in the nonmagnetic case, while it is the *OH reduction (*OH \rightarrow $H_2O(l))$ in the latter case. Though it is well known that the spin-unpolarized DFT method is not recommended to study catalytic processes, our test computation here provides another example that such a computational method is not reliable to examine reaction pathways.

3.4. Linear relationship between limiting potential and key descriptors

Our above analyses clearly showed that it is important to well consider the magnetic coupling between two transition metal atoms in DACs, and the spin-polarized DFT computations involving magnetic coupling give more accurate prediction of the catalytic activity of these DACs. As shown in Fig. 5a, when the magnetic coupling is considered, the limiting potentials of the 10 DACs are higher, especially better catalytic

performance is predicted for CoMN $_6$ -gra(OH) (M = Ni, Cu, Zn) catalysts than the previously reported [48–51].

In order to better understand the role played by magnetic coupling in DACs, and also to find the characteristic descriptors of the 4e-pathway of ORR, we examined the relationship between the limiting potential ($U_{\rm L}$) and key descriptors, such as $\Delta G_{^{*}\rm OH}$ and outer d-electron number of M atom (Fig. 5b and c). Since Ref. 51 only examined six out of the 10 catalysts examined here, we also fitted our own data for these six catalysts, which are indicated by dashed lines in Fig. 5b and c.

Many previous studies indicated that the ORR activity is mainly determined by the free energy changes of *OOH, *O and *OH species, and the ORR catalytic activity and adsorption free energies form a volcano plot [93]. Thus, we first examined the relationship between the catalytic activity and $\Delta G_{^*OH}$. Regardless of whether the magnetic

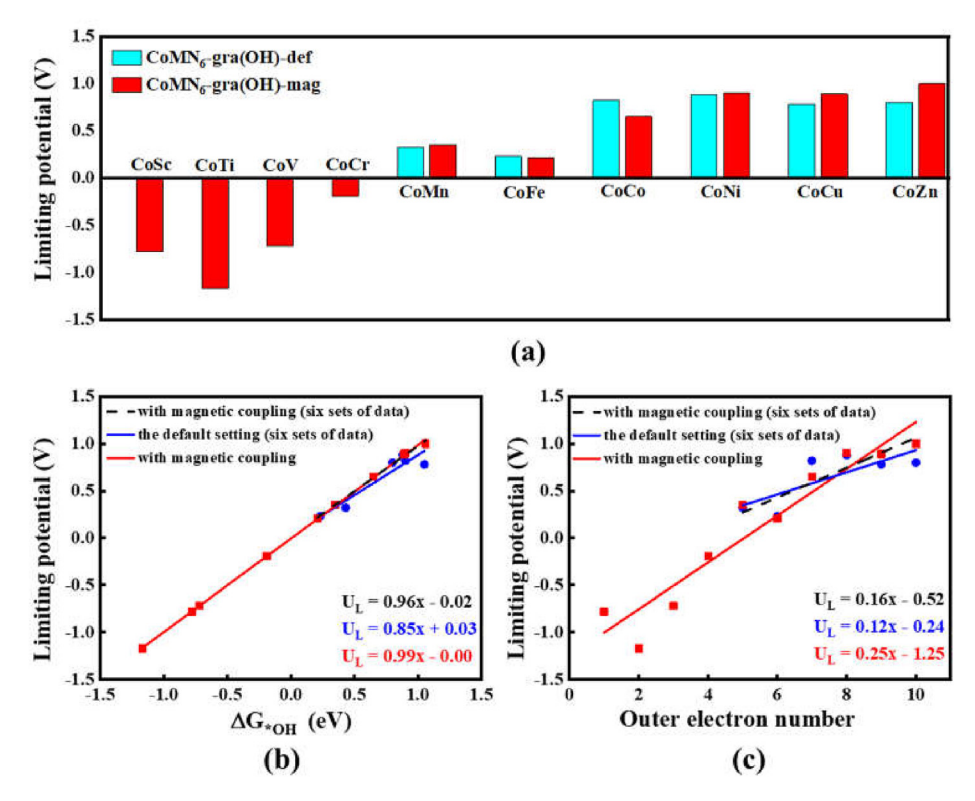


Fig. 5. Histogram of limiting potentials of ten DACs in magnetic default setting and with magnetic coupling (a), linear fitting of limiting potential with $\Delta G_{^{\circ}OH}$ (b) and outer d-electron number of M (c) in magnetic default setting, with magnetic coupling and part of with magnetic coupling, respectively.

coupling is considered or not, U_L and $\Delta G_{^*OH}$ of the 10 DACs have a linear relationship (Fig. 5b), but the linear fitting is better when the magnetic coupling is well treated (Pearson correlation coefficient (ρ) of 0.999 vs. 0.943). If we only limited to the six catalysts in Ref. [51], the linear relationship is also better upon including the magnetic coupling (ρ value 0.998 vs. 0.943, for the data indicated by the dashed lines in Fig. 5b).

We next investigated the relationship between the catalytic activity and the outer d-electron number of M atom in the DACs. Interestingly, nearly the same trend was obtained as that between U_L and $\Delta G_{^{*}OH}$. Better linear fitting is obtained when the magnetic coupling is well considered as compared with the case only default magnetic setting is used (for the 10 DACs, ρ value 0.952 vs. 0.771; for the six catalysts in Ref.51, ρ value 0.914 vs. 0.771, for the data indicated by the dashed lines in Fig. 5c).

The above results showed that considering magnetic coupling gives better linear fitting between the activity and the key descriptors. Thus, considering the magnetic coupling is essential to precisely predict the catalytic ORR performance of DACs, when the descriptor-based procedure is used to screen potential DACs.

3.5. Origin of ORR activity

To investigate the origin of magnetic configuration changes in the catalyst and how the magnetic coupling impacts on the ORR performance, we calculated the Bader charge of the key intermediates (Table S11). It was found that the charge transfer occurs between the transition metal and the adsorbate in each step of the reaction, and the amount of the transferred charge associates with the activation of the adsorbed species by the catalyst. All the transition metals on DACs are positively charged, but the two metal atoms of the same catalyst have different amounts of positive charge partially due to the synergistic interaction between adjacent transition metal atoms, which may play an important role in tuning the electronic structures of the active metal centers in the catalytic process [46].

Since CoMN₆-gra(OH) (M = Ni, Cu, Zn) catalysts have exceptional

catalytic activity towards ORR (with η_{ORR} values of 0.33, 0.34 and 0.23 V, respectively), we carefully examined the charge transfer on these three catalysts. As shown in Table S11, pronounced charge change occurs on the Co site along the elementary reaction steps, while the charge on the M (M = Ni, Cu, Zn) site has very little change. The corresponding changes in the magnetic moments on Co in these three catalysts are also more remarkable (Table S11). The asymmetric charge distribution on the active site may be one of the reasons for its excellent catalytic performance [22].

Then, we investigated the effect of magnetic coupling on the potential limiting step of three distinguished DACs, namely CoMN₆-gra(OH) (M = Ni, Cu, Zn). As shown in Table S10, on CoNiN₆-gra(OH), regardless whether the magnetic coupling is well considered or not, the limiting step is the process of *OH \rightarrow H₂O(l). This is why the limiting potential in our calculations after considering magnetic coupling (0.33 V) is similar to that obtained by Deng et al. (0.35 V) when the magnetic configuration was set as default value) [51]. However, for CoCuN6-gra(OH) and CoZnN₆-gra(OH), the potential limiting steps are different from the previous studies [51]. When the magnetic coupling was well considered, the PDSs are *OH (NM) \rightarrow H₂O(l) (FM) and *O (FM) \rightarrow *OH (NM), respectively, both are accompanied by changes in magnetic coupling; while when the magnetic properties were set to default values, the PDSs are $O_2(g) \to {}^*OOH$ and ${}^*OH \to H_2O(l),$ respectively. Such differences may be the main reason for the improvement of ORR catalytic activity after well considering the magnetic coupling between transition metal

To further elucidate the underlying reason for the enhanced catalytic activity by the pre-adsorbed OH species and considering the magnetic coupling, we plotted the density of states (DOS) for the 10 examined DACs with or without pre-adsorption of *OH groups, and with default magnetism setting or magnetic coupling (Fig. 6 and Fig. S3). All these 10 DACs have electronic DOS at the Fermi energy level (0 eV), and thus are metallic. When magnetic coupling is considered, the *OH-adsorbed DACs have more bimetallic overlap in the DOS diagram than the pristine

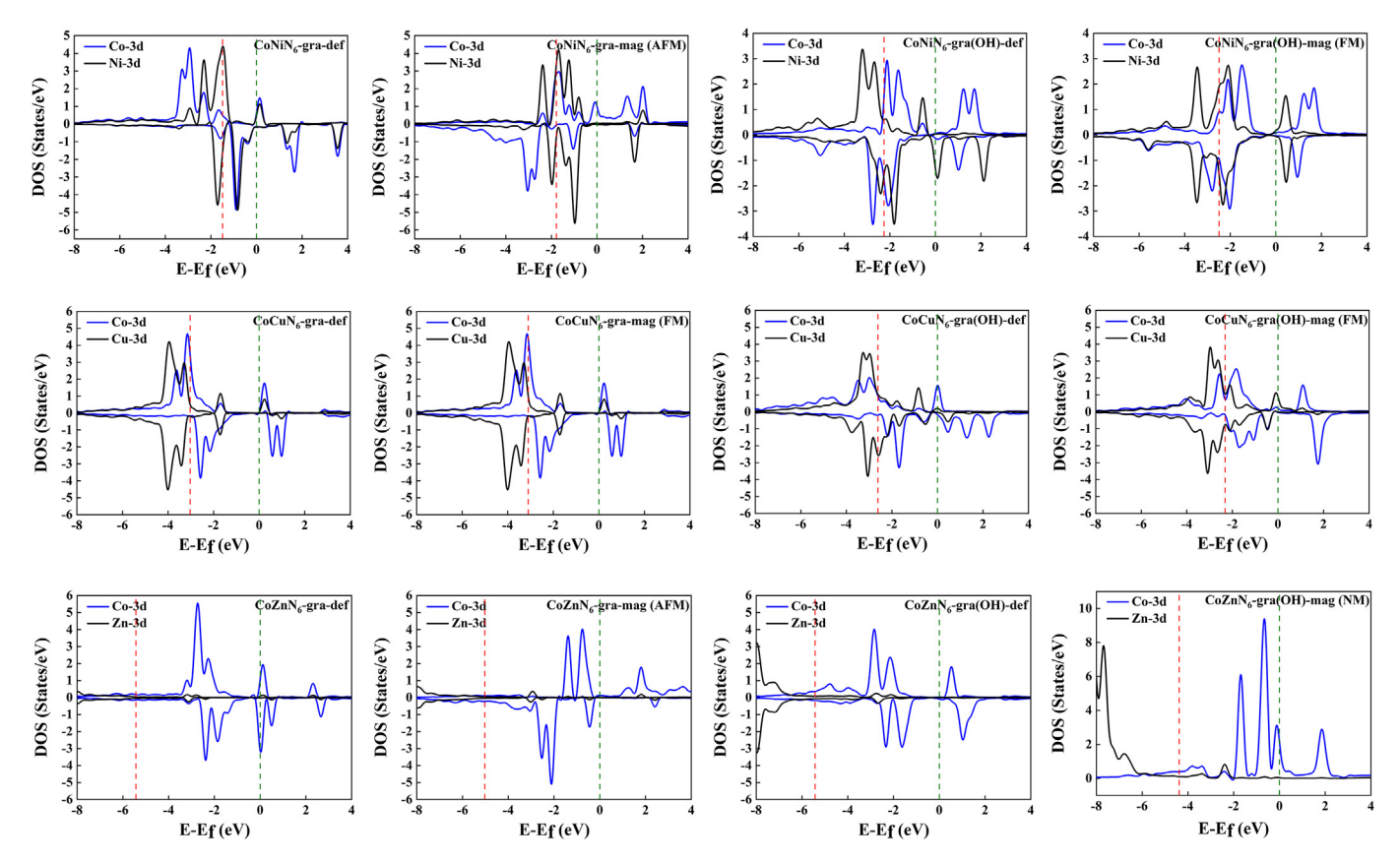


Fig. 6. Density of States plot for $CoNiN_6$ -gra(OH), $CoCuN_6$ -gra(OH) and $CoZnN_6$ -gra(OH) with or without pre-adsorption of *OH groups with default magnetism setting and magnetic coupling, where the green and red dashed lines indicate the Fermi energy level and the d-band center, respectively. The magnetic ground state when well considering magnetic coupling is given in parentheses.

counterparts have, especially for $CoNiN_6$ -gra(OH) and $CoFeN_6$ -gra(OH) DACs, which indicates that the *OH-adsorption introduces a stronger interaction between the two metal atoms.

In addition, when magnetic coupling is considered, the contributions of metal atoms at the Fermi energy level are different in the DACs after adsorption of *OH groups, as compared with that using the magnetic default setting. For example, for the CoCuN₆-gra(OH), the Cu atom is the main contributor when magnetic coupling is considered, while the Co atom dominates the DOS when using the default magnetism setting; for the CoZnN₆-gra(OH), Co contributes more than Zn does with either default setting or magnetic coupling, while the contribution of Co atoms is obviously enhanced when magnetic coupling is considered.

According to Sabatier's principle, an ideal catalyst should provide a moderate adsorption strength for reactants, intermediates, and products, so that these species can leave the active site when the catalytic reaction is complete [56,79]. The adsorption strength on the catalyst is related to the d-band center: the closer the d-band center is to the Fermi energy level, the stronger the adsorption of the adsorbate to the catalyst. Thus, including pre-adsorbed OH species and magnetic coupling or not is expected to affect the position of the d-band center.

Thus, we calculated the *d*-band centers of these catalysts (Table 2) with or without pre-adsorption of *OH groups (Table 2). Regardless whether the magnetic coupling is considered or not, compared with the pristine CoMN₆-gra, in most of the CoMN₆-gra(OH) catalysts, the *d*-band centers are further away from the Fermi level, the significant exception is CoZnN₆-gra whose *d*-band center is far away from the Fermi level, upon the adsorption of *OH group, the *d*-band shifts closer to the Fermi level. Thus, the pre-adsorption of *OH in general pushes the *d*-band center away from the Fermi level, resulting in a milder adsorption of the adsorbate, and the enhanced catalytic activity of these DACs.

Including magnetic coupling or not will affect the d-band centers of

Table 2 *d*-band centers ($C_{d\text{-band}}$, in eV) of CoMN₆-gra and CoMN₆-gra(OH) with default setting of magnetic and with magnetic coupling.

	$C_{d\text{-band}}$ with magnetic coupling	$C_{d ext{-band}}$ with default setting
CoSc/CoSc(OH)	0.03/-0.17	0.11/0.30
CoTi/CoTi(OH)	-0.39/-0.34	0.03/-0.21
CoV/CoV(OH)	-0.97/-1.05	-0.54/-0.79
CoCr/CoCr(OH)	-1.14/-1.05	-0.60/-0.84
CoMn/CoMn(OH)	-1.61/-1.88	-1.02/-1.35
CoFe/CoFe(OH)	-1.21/-1.94	-1.39/-1.79
CoCo/CoCo(OH)	-1.45/-1.69	-1.96/-1.48
CoNi/CoNi(OH)	-1.78/-2.49	-1.49/-2.26
CoCu/CoCu(OH)	-3.10/-2.32	-3.03/-2.61
CoZn/CoZn(OH)	-5.03/-4.38	-5.43/-5.04

the DACs under examination. When the magnetic coupling is considered, for most of the CoMN $_6$ -gra(OH) catalysts, the d-band center shifts to lower energy, while the opposite happens for CoZnN $_6$ -gra(OH) whose d-band center is too far away from the Fermi level at the default magnetic setting. Including the magnetic coupling pushes the d-band center to a higher energy level (closer to the Fermi level). In general, after considering the magnetic coupling, the d-band center moves to the position which favors a modest binding strength between catalyst and adsorbate, resulting in the promoted ORR catalytic activity.

4. Conclusions

In summary, the catalytic performance of 10 Co-based double-atom catalysts, $CoMN_6$ -gra (M = Sc, Ti, V, Cr, Mn, Fe, Co, Ni, Cu, Zn), toward ORR was revisited by the first-principles calculations, emphasizing the necessity of including the magnetic coupling between the two metal

atoms. The spin-polarized DFT computations were performed with magnetic coupling, and those with default magnetic states were carried out for comparison. Different computational approaches predict different limiting potentials and different order of electrocatalytic performance toward ORR, largely because the magnetic coupling between transition metal atoms affects the binding strength between intermediates and DACs, the potential determining step, and the limiting potential. The ORR catalytic activity of these DACs is highly correlated with the number of outer electrons and the d-band center, which provide guidelines for designing related DACs toward ORR. This work revealed that it is of critical importance to consider magnetic coupling between transition metal atoms and examine the spin states of catalyst active sites and reaction intermediates for accurate prediction of catalytic performance of DACs, and demonstrated that manipulating the magnetic coupling between transition metal atoms is an emerging and effective approach to enhance the electrocatalytic activity of DACs. Note that the above conclusions hold true also for tri-atom catalysts, single-cluster catalysts, and even metal-free catalysts, and for reactions beyond ORR. Also note that the magnetic coupling associates with charge, structure, symmetry, component elements, interlayer interaction, external field, etc. [94]. We hope that this work will stimulate more efforts in designing efficient nanocatalysts by manipulating magnetic coupling in both theoretical and experimental communities.

Declaration of competing interest

The authors declare that they have no known competing financial interests or personal relationships that could have appeared to influence the work reported in this paper.

Acknowledgements

This work was financially supported in China by the National Natural Science Foundation of China (Grant Nos. 11704203, 11964024), the "Grassland Talents" project of Inner Mongolia Autonomous Region, China (Grant No. 12000-12102613), the Young Science and Technology Talents Cultivation Project of Inner Mongolia University, China (21221505), and the computational support from PARATEAR, and in USA by the National Science Foundation-Centers of Research Excellence in Science and Technology (NSF-CREST Center) for Innovation, Research and Education in Environmental Nanotechnology (CIRE2N) (Grant No. HRD-1736093). We thank Prof. Qing Tang and Dr. Chaofang Deng at Chongqing University for constructive discussions.

Appendix A. Supplementary data

Supplementary data to this article can be found online at https ://doi.org/10.1016/j.apmate.2022.01.004.

References

- [1] Y. Yang, R. Zhao, T. Zhang, K. Zhao, P. Xiao, Y. Ma, P.M. Ajayan, G. Shi, Y. Chen, Graphene-based standalone solar energy converter for water desalination and purification, ACS Nano 12 (2018) 829-835.
- [2] G. Feng, L. An, B. Li, Y. Zuo, J. Song, F. Ning, N. Jiang, X. Cheng, Y. Zhang, D. Xia, Atomically ordered non-precious Co₃Ta intermetallic nanoparticles as highperformance catalysts for hydrazine electrooxidation, Nat. Commun. 10 (2019)
- [3] E.L.V. Eriksson, E.M. Grav. Optimization and integration of hybrid renewable energy hydrogen fuel cell energy systems - A critical review, Appl. Energy 202 (2017) 348-364.
- [4] S. Smeets, L.B. McCusker, C. Baerlocher, D. Xie, C. Chen, S.I Zones, SSZ-87: a borosilicate zeolite with unusually flexible 10-ring pore openings, J. Am. Chem. Soc. 137 (2015) 2015-2020.
- M. Winter, R. Brodd, What are batteries, fuel cells, and supercapacitors? Chem. Rev. 104 (2004) 4245-4269.
- D. Zhang, F. Wu, M. Peng, X. Wang, D. Xia, G. Guo, One-step, facile and ultrafast synthesis of phase- and size-controlled Pt-Bi intermetallic nanocatalysts through continuous flow microfluidics, J. Am. Chem. Soc. 137 (2015) 6263-6269.

- [7] I. Staffell, D. Scamman, A.V. Abad, P. Balcombe, P.E. Dodds, P. Ekins, N. Shahd, K.R. Ward, The role of hydrogen and fuel cells in the global energy system, Energy Environ. Sci. 12 (2019) 463.
- X. Chen, S. Huang, F. Sun, N. Lai, Modifications of metal and ligand to modulate the oxygen reduction reaction activity of two-dimensional MOF catalysts, J. Phys. Chem. C 124 (2020) 1413-1420.
- A.A. Gewirth, J.A. Varnell, A.M. DiAscro, Nonprecious metal catalysts for oxygen reduction in heterogeneous aqueous systems, Chem. Rev. 118 (2018) 2313-2339.
- [10] A. Kulkarni, S. Siahrostami, A. Patel, J.K. Nørskov, Understanding catalytic activity trends in the oxygen reduction reaction, Chem. Rev. 118 (2018) 2302-2312.
- P.C.K. Vesborg, T.F. Jaramillo, Addressing the terawatt challenge: scalability in the supply of chemical elements for renewable energy, RSC Adv. 2 (2012) 7933-7947.
- [12] J.X. Flores-Lasluisa, D. Salinas-Torres, M.V. López-Ramón, M.A. Álvarez, C. Moreno-Castilla, D. Cazorla-Amorós, E. Morallón, Copper ferrite nanospheres composites mixed with carbon black to boost the oxygen reduction reaction, Colloids Surf. A Physicochem. Eng. Asp. 613 (2021), 126060.
- [13] Y. Wang, Y. Li, T. Heine, PtTe monolayer: two-dimensional electrocatalyst with high basal plane activity toward oxygen reduction reaction, J. Am. Chem. Soc. 140 (2018) 12732-12735.
- [14] C. Deng, F. Li, Q. Tang, Electrocatalytic oxygen reduction reaction over the Au₂₂(L⁸)₆ nanocluster with promising activity: A DFT study, J. Phys. Chem. C 123 (2019) 27116–27123.
- [15] S. Yia, H. Jianga, X. Baoa, S. Zoua, J. Liaoc, Z. Zhang, Recent progress of Pt-based catalysts for oxygen reduction reaction in preparation strategies and catalytic mechanism, J. Electroanal. Chem. 848 (2019), 113279.
- [16] M. Liu, Z. Zhao, X. Duan, Y. Huang, Nanoscale structure design for highperformance Pt-based ORR catalysts, Adv. Mater. 31 (2019) 1802234.
- C. Wang, N.M. Markovic, V.R. Stamenkovic, Advanced platinum alloy electrocatalysts for the oxygen reduction reaction, ACS Catal. 2 (2012) 891-898.
- [18] A. Russell, Electrocatalysis: theory and experiment at the interface, Phys. Chem. Chem. Phys. 10 (2008) 3722-3730.
- [19] Z. Duan, G. Wang, A first principles study of oxygen reduction reaction on a Pt(111) surface modified by a subsurface transition metal M (M = Ni, Co. or Fe). Phys. Chem. Chem. Phys. 13 (2011) 20178-20187.
- S. Wang, L. Zhang, Z. Xia, A. Roy, D.W. Chang, J. Baek, L. Dai, BCN graphene as efficient metal-free electrocatalyst for the oxygen reduction reaction, Angew. Chem. Int. Ed. 51 (2012) 4209-4212.
- [21] Y. Yuan, J. Ma, H. Ai, B. Kang, J.Y. Lee, A simple general descriptor for rational design of graphyne-based bifunctional electrocatalysts toward hydrogen evolution and oxygen reduction reactions, J. Colloid Interface Sci. 592 (2021) 440-447.
- [22] Q. Guo, J. Feng, D. Chen, N. Song, H. Dong, L. Yu, L. Dong, Theoretical insights into enhanced electrocatalytic activity of oxygen reduction reactions on N/S-codoped graphene quantum dots, J. Phys. Chem. C 125 (2021) 9747–9755.
 [23] X. Xue, H. Meng, Z. Huang, Y. Feng, X. Qi, Black phosphorus-based materials for
- energy storage and electrocatalytic applications, J. Phys. Energy 3 (2021), 042002.
- [24] X. Xue, S. Shen, X. Jiang, P. Sengdala, K. Chen, Y. Feng, Tuning the catalytic property of phosphorene for oxygen evolution and reduction reactions by changing oxidation degree, J. Phys. Chem. Lett. 10 (2019) 3440-3446.
- [25] F. Chang, Z. Bai, M. Li, M. Ren, T. Liu, L. Yang, C. Zhong, J. Lu, Strain-modulated platinum-palladium nanowires for oxygen reduction reaction, Nano Lett. 20 (2020) 2416-2422.
- Y. Zhao, L. Tao, W. Dang, L. Wang, M. Xia, B. Wang, M. Liu, F. Gao, J. Zhang, Y. Zhao, High-indexed PtNi alloy skin spiraled on Pd nanowires for highly efficient oxygen reduction reaction catalysis, Small 15 (2019), 1900288.
- [27] Z. Sadighi, J. Liu, L. Zhao, F. Ciucci, J. Kim, Metallic MoS₂ nanosheets: Multifunctional electrocatalyst for the ORR, OER and Li-O2 batteries, Nanoscale 10 (2018) 22549.
- [28] Y. Chen, S. Tian, Q. Tang, First-principles studies on electrocatalytic activity of novel two-dimensional MA2Z4 monolayers toward oxygen reduction reaction, J. Phys. Chem. C 125 (2021) 22581-22590.
- [29] H. Osgood, S.V. Devaguptapu, H. Xu, J. Cho, G. Wu, Transition metal (Fe, Co, Ni, and Mn) oxides for oxygen reduction and evolution bifunctional catalysts in alkaline media, Nano Today 11 (2016) 601-625.
- [30] L. Qian, Z. Lu, T. Xu, X. Wu, Y. Tian, Y. Li, Z. Huo, X. Sun, X. Duan, Trinary layered double hydroxides as high-performance bifunctional materials for oxygen electrocatalysis, Adv. Energy Mater. 5 (2015) 1-6.
- [31] F. Sun, C. Deng, S. Tian, Q. Tang, Oxygen electrocatalysis by [Au₂₅(SR)₁₈]: Charge, doping, and ligand removal effect, ACS Catal. 11 (2021) 7957-7969.
- [32] X. Guo, X. Hu, D. Wu, C. Jing, W. Liu, Z. Ren, Q. Zhao, X. Jiang, C. Xu, Y. Zhang, N. Hu, Tuning the bifunctional oxygen electrocatalytic properties of core-shell Co₃O₄@NiFe LDH catalysts for Zn-Air batteries: Effects of interfacial cation valences, ACS Appl. Mater. Interfaces 11 (2019) 21506-21514.
- [33] Y. Ha, L. Shi, X. Yan, Z. Chen, Y. Li, W. Xu, R. Wu, Multifunctional electrocatalysis on a porous N-doped NiCo2O4@C nanonetwork, ACS Appl. Mater. Interfaces 11 (2019) 45546-45553.
- B. Qiao, A. Wang, X. Yang, L.F. Allard, Z. Jiang, Y. Cui, J. Liu, J. Li, T. Zhang, Singleatom catalysis of CO oxidation using Pt₁/FeO_x, Nat. Chem. 3 (2011) 634-641.
- [35] R.K. Ahluwalia, X. Wang, L. Osmieri, J.-K. Peng, C.F. Cetinbas, J. Park, D.J. Myers, H.T. Chung, K.C. Neyerlin, Stability of atomically dispersed Fe-N-C ORR catalyst in polymer electrolyte fuel cell environment, J. Electrochem. Soc. 168 (2021), 024513.
- [36] Z. Li, H. He, H. Cao, S. Sun, W. Diao, D. Gao, P. Lu, S. Zhang, Z. Guo, M. Li, R. Liu, D. Ren, C. Liu, Y. Zhang, Z. Yang, J. Jiang, G. Zhang, Atomic Co/Ni dual sites and Co/Ni alloy nanoparticles in N-doped porous janus-like carbon frameworks for bifunctional oxygen electrocatalysis, Appl. Catal., B 240 (2019) 112-121.

- [37] H.T. Chung, D.A. Cullen, D. Higgins, B.T. Sneed, E.F. Holby, K.L. More, P. Zelenay, Direct atomic-level insight into the active sites of a high-performance PGM-free ORR catalyst, Science 357 (2017) 479–484.
- [38] C. Zhu, Q. Shi, B.Z. Xu, S. Fu, G. Wan, C. Yang, S. Yao, J. Song, H. Zhou, D. Du, S.P. Beckman, D. Su, Y. Lin, Hierarchically porous M-N-C (M = Co and Fe) single-atom electrocatalysts with robust MN_x active moieties enable enhanced ORR performance, Adv. Energy Mater. 8 (2018), 1801956.
- [39] J.M. Ziegelbauer, T.S. Olson, S. Pylypenko, F. Alamgir, C. Jaye, P. Atanassov, S. Mukerjee, Direct spectroscopic observation of the structural origin of peroxide generation from Co-based pyrolyzed porphyrins for ORR applications, J. Phys. Chem. C 112 (2008) 8839–8849.
- [40] H. Jing, P. Zhu, X. Zheng, Z. Zhang, D. Wang, Y. Li. Theory-oriented screening and discovery of advanced energy transformation materials in electrocatalysis, Adv. Powder Mater. DOI: 10.1016/j.apmate.2021.10.004.
- [41] F. Ling, W. Xia, L. Li, X. Zhou, X. Luo, Q. Bu, J. Huang, X. Liu, W. Kang, M. Zhou, Single transition metal atom bound to the unconventional phase of the MoS₂ monolayer for catalytic oxygen reduction reaction: A first-principles study, ACS Appl. Mater. Interfaces 13 (2021) 17412–17419.
- [42] F. Li, X. Liu, Z. Chen, 1+1' > 2: heteronuclear Biatom catalyst outperforms its homonuclear counterparts for CO oxidation, Small Methods 3 (2019) 1800480.
- [43] Y. Pan, C. Zhang, Z. Liu, C. Chen, Y. Li, Structural regulation with atomic-level precision: From single-atomic site to diatomic and atomic interface catalysis, Matter 2 (2020) 78–110.
- [44] Y. Ying, X. Luo, J. Qiao, H. Huang, "More is different:" Synergistic effect and structural engineering in double-atom catalysts, Adv. Funct. Mater. 31 (2020) 3.
- [45] M. Xiao, H. Zhang, Y. Chen, J. Zhu, L. Gao, Z. Jin, J. Ge, Z. Jiang, S. Chen, C. Liu, W. Xing, Identification of binuclear Co₂N₅ active sites for oxygen reduction reaction with more than one magnitude higher activity than single atom CoN₄ Site, Nano Energy 48 (2018) 396–403.
- [46] X. Zhu, D. Zhang, C. Chen, Q. Zhang, R. Liu, Z. Xia, L. Dai, R. Amal, X. Lu, Harnessing the interplay of Fe-Ni atom pairs embedded in nitrogen-doped carbon for bifunctional oxygen electrocatalysis, Nano Energy 71 (2020), 104597.
- [47] W. Ye, S. Chen, Y. Lin, L. Yang, S. Chen, X. Zheng, Z. Qi, C. Wang, R. Long, M. Chen, J. Zhu, P. Gao, L. Song, J. Jiang, Y. Xiong, Precisely tuning the number of Fe atoms in clusters on N-doped carbon toward acidic oxygen reduction reaction, Inside Chem. 5 (2019) 2865–2878.
- [48] X. Han, X. Ling, D. Yu, D. Xie, L. Li, S. Peng, C. Zhong, N. Zhao, Y. Deng, W. Hu, Atomically dispersed binary Co—Ni sites in nitrogen-doped hollow carbon nanocubes for reversible oxygen reduction and evolution, Adv. Mater. 31 (2019) 1905622.
- [49] Z. Lu, B. Wang, Y. Hu, W. Liu, Y. Zhao, R. Yang, Z. Li, J. Luo, B. Chi, Z. Jiang, M. Li, S. Mu, S. Liao, J. Zhang, X. Sun, An isolated zinc—cobalt atomic pair for highly active and durable oxygen reduction, Angew. Chem. Int. Ed. 58 (2019) 2622–2626.
- [50] D. Zhang, L. Gong, J. Ma, X. Wang, L. Zhang, Z. Xia, Disperse multimetal atom-doped carbon as efficient bifunctional electrocatalysts for oxygen reduction and evolution reactions: Design strategies, J. Phys. Chem. C 124 (2020) 27387–27395.
- [51] C. Deng, Y. Su, F. Li, W. Shen, Z. Chen, Q. Tang, Understanding activity origin for the oxygen reduction reaction on bi-atom catalysts by DFT studies and machinelearning, J. Mater. Chem. A 8 (2020) 24563–24571.
- [52] X. Zhu, J. Yan, M. Gu, T. Liu, Y. Dai, Y. Gu, Y. Li, Activity origin and design principles for oxygen reduction on dualmetal-site catalysts: A combined density functional theory and machine learning study, J. Phys. Chem. Lett. 10 (2019) 7760–7766
- [53] P. Roy, A. Pramanik, P. Sarkar, Graphitic carbon nitride sheet supported singleatom metal-free photocatalyst for oxygen reduction reaction: A first-principles analysis, J. Phys. Chem. Lett. 12 (2021) 2788–2795.
- [54] X. Chen, S. Lin, S. Qing, Y. Zhang, X. Li, Density functional theory study of the sulfur/oxygen doped CoN_4 —graphene electrocatalyst for oxygen reduction reaction, Colloids Surf. A Physicochem. Eng. Asp. 615 (2021), 126219.
- [55] J. Xu, A. Elangovan, J. Li, B. Liu, Graphene-based dual-metal sites for oxygen reduction reaction: A theoretical study, J. Phys. Chem. C 125 (2021) 2334–2344.
- [56] M. Xiao, Y. Chen, J. Zhu, H. Zhang, X. Zhao, L. Gao, X. Wang, J. Zhao, J. Ge, Z. Jiang, S. Chen, C. Liu, W. Xing, Climbing the apex of the ORR volcano plot via binuclear site construction: Electronic and geometric engineering, J. Am. Chem. Soc. 141 (2019) 17763–17770.
- [57] C. Deng, W. Li, R. He, W. Shen, M. Li, Understanding and breaking the scaling relations in the oxygen reduction reaction on Pd_xCu_{4-x} subnanoclusters supported by defective two-dimensional boron nitride materials, J. Phys. Chem. C 124 (2020) 19530–19537.
- [58] J. Zhang, Y. Zhao, C. Chen, Y. Huang, C. Dong, C. Chen, R. Liu, C. Wang, K. Yan, Y. Li, G. Wang, Tuning the coordination environment in single-atom catalysts to achieve highly efficient oxygen reduction reactions, J. Am. Chem. Soc. 141 (2019) 20118–20126.
- [59] F. Liu, G. Zhu, D. Yang, D. Jia, F. Jin, W. Wang, Systematic exploration of N,C configurational effects on the ORR performance of Fe-N doped graphene catalysts based on DFT Calculations, RSC Adv. 9 (2019) 22656-22667.
- [60] X. Zhang, Z. Yang, Z. Lu, W. Wang, Bifunctional CoN_x embedded graphene electrocatalysts for OER and ORR: A theoretical evaluation, Carbon 130 (2018) 112-119
- [61] S.N. Reddy, C.B. Krishnamurthy, I. Grinberg, First-principles study of the ligand substituent effect on ORR catalysis by metallocorroles, J. Phys. Chem. C 124 (2020) 11275–11283.
- [62] L. Li, Y. Li, R. Huang, X. Cao, Y. Wen, Boosting the electrocatalytic activity of Fe—Co dual-atom catalysts for oxygen reduction reaction by ligand-modification engineering, ChemCatChem 13 (2021) 4645–4651.

- [63] C. Tang, L. Chen, H. Li, L. Li, Y. Jiao, Y. Zheng, H. Xu, K. Davey, S. Qiao, Tailoring acidic oxygen reduction selectivity on single-atom catalysts via modification of first and second coordination spheres, J. Am. Chem. Soc. 143 (2021) 7819–7827.
- [64] Q. Li, X. Li, G. Zhang, J. Jiang, Cooperative spin transition of monodispersed FeN₃ sites within graphene induced by CO adsorption, J. Am. Chem. Soc. 140 (2018) 15149–15152.
- [65] Y. Gong, W. Zhong, Y. Li, Y. Qiu, L. Zheng, J. Jiang, H. Jiang, Regulating photocatalysis by spin-state manipulation of cobalt in covalent organic frameworks, J. Am. Chem. Soc. 142 (2020) 16723–16731.
- [66] W. Zhong, Y. Qiu, H. Shen, X. Wang, J. Yuan, C. Jia, S. Bi, J. Jiang, Electronic spin moment as a catalytic descriptor for Fe single-atom catalysts supported on C₂N, J. Am. Chem. Soc. 143 (2021) 4405–4413.
- [67] Q. Dang, S. Tang, T. Liu, X. Li, X. Wang, W. Zhong, Y. Luo, J. Jiang, Regulating electronic spin moments of single-atom catalyst sites via single-atom promoter tuning on s-vacancy MoS₂ for efficient nitrogen fixation, J. Phys. Chem. Lett. 12 (2021) 8355–8362.
- [68] H. Li, Z. Zhao, Q. Cai, L. Yin, J. Zhao, Nitrogen electroreduction performance of transition metal dimers embedded into N-doped graphene: A theoretical prediction, J. Mater. Chem. A 8 (2020) 4533–4543.
- [69] J. Wang, Z. Huang, W. Liu, C. Chang, H. Tang, Z. Li, W. Chen, C. Jia, T. Yao, S. Wei, Y. Wu, Y. Li, Design of N-coordinated dual-metal sites: A stable and active Pt-free catalyst for acidic oxygen reduction reaction, J. Am. Chem. Soc. 139 (2017) 17281–17284.
- [70] J. Zhao, X. Huang, P. Jin, Z. Chen, Magnetic properties of atomic clusters and endohedral metallofullerenes, Coord. Chem. Rev. 289–290 (2015) 315–340.
- [71] G.G. Kresse, J.J. Furthmüller, Efficient iterative schemes for ab initio total-energy calculations using a plane-wave basis set, Phys. Rev. B 54 (1996) 11169–11186.
- [72] G.G. Kresse, J.J. Furthmüller, Efficiency of ab-initio total energy calculations for metals and semiconductors using a plane-wave basis set, Comput. Mater. Sci. 6 (1996) 15–50.
- [73] P.E. Blöchl, Projector augmented-wave method, Phys. Rev. B 50 (1994) 17953–17979.
- [74] J.P. Perdew, K. Burke, M. Ernzerhof, Generalized gradient approximation made simple, Phys. Rev. Lett. 77 (1996) 3865–3868.
- [75] C. Chowdhury, A. Datta, Silicon-doped nitrogen-coordinated graphene as electrocatalyst for oxygen reduction reaction, J. Phys. Chem. C 122 (2018) 27233–27240.
- [76] T. Bučko, J. Hafner, S. Lebègue, J.G. Ángyán, Improved description of the structure of molecular and layered crystals: Ab initio DFT calculations with van der waals corrections, J. Phys. Chem. A 114 (2010) 11814–11824.
- [77] S.L. Dudarev, G.A. Botton, S.Y. Savrasov, C.J. Humphreys, A.P. Sutton, Electronenergy-loss spectra and the structural stability of nickel oxide: An LSDA+U study, Phys. Rev. B Phys. 57 (1998) 1505.
- [78] K. Mathew, R. Sundararaman, K. Letchworth-Weaver, T.A. Arias, R.G. Hennig, Implicit solvation model for density-functional study of nanocrystal surfaces and reaction pathways, J. Chem. Phys. 140 (2014), 084106.
- [79] H. Zeng, X. Liu, F. Chen, Z. Chen, X. Fan, W. Lau, Single atoms on a nitrogen-doped boron phosphide monolayer: A new promising bifunctional electrocatalyst for ORR and OER, ACS Appl. Mater. Interfaces 12 (2020) 52549–52559.
- [80] X. Guo, J. Gu, S. Lin, S. Zhang, Z. Chen, S. Huang, Tackling the activity and selectivity challenges of electrocatalysts toward the nitrogen reduction reaction via atomically dispersed biatom catalysts, J. Am. Chem. Soc. 142 (2020) 5709–5721.
- [81] I.C. Man, H. Su, F. Calle-Vallejo, H.A. Hansen, J.I. Martínez, N.G. Inoglu, J. Kitchin, T.F. Jaramillo, J.K. Nørskov, J. Rossmeisl, Universality in oxygen evolution electrocatalysis on oxide surfaces, ChemCatChem 3 (2011) 1159–1165.
- [82] Z. Shao, H. Meng, J. Sun, N. Guo, H. Xue, K. Huang, F. He, F. Li, Q. Wang, Engineering of amorphous structures and sulfur defects into ultrathin FeS nanosheets to achieve superior electrocatalytic alkaline oxygen evolution, ACS Appl. Mater. Interfaces 12 (2020) 51846–51853.
- [83] M. Gao, X. Cao, Q. Gao, Y. Xu, Y. Zheng, J. Jiang, S. Yu, Nitrogen-doped graphene supported CoSe₂ nanobelt composite catalyst for efficient water oxidation, ACS Nano 8 (2014) 3970–3978.
- [84] J. Sun, N. Guo, Z. Shao, K. Huang, Y. Li, F. He, Q. Wang, A facile strategy to construct amorphous spinel-based electrocatalysts with massive oxygen vacancies using ionic liquid dopant, Adv. Energy Mater. 8 (2018), 1800980.
- [85] Y. Meng, C. Yin, K. Li, H. Tang, Y. Wang, Z. Wu, Improved oxygen reduction activity in heteronuclear FeCo-codoped graphene: A theoretical study, ACS Sustain. Chem. Eng. 7 (2019) 17273–17281.
- [86] S. Liu, L. Cheng, W. Wang, K. Li, Y. Wang, Z. Wu, Fe-porphyrin carbon matrix as a bifunctional catalyst for oxygen reduction and CO₂ reduction from theoretical perspective, Mol. Phys. 117 (2018) 1–8.
- [87] M.A. Hunter, J.M.T.A. Fischer, Q. Yuan, M. Hankel, D.J. Searles, Evaluating the catalytic efficiency of paired, single-atom catalysts for the oxygen reduction reaction, ACS Catal. 9 (2019) 7660–7667.
- [88] X. Yang, D. Xia, Y. Kang, H. Du, F. Kang, L. Gan, J. Li, Unveiling the axial hydroxyl ligand on Fe-N₄-C electrocatalysts and its impact on the pH-dependent oxygen reduction activities and poisoning kinetics, Adv. Sci. 7 (2020), 2000176.
- [89] H.T. Chung, D.A. Cullen, D. Higgins, B.T. Sneed, E.F. Holby, K.L. More, P. Zelenay, Direct atomic-level insight into the active sites of a high-performance PGM-free ORR catalyst, Science 357 (2017) 479–484.
- [90] Y. Zhao, J. Gu, Z. Chen, Oxygen evolution reaction on 2D ferromagnetic Fe₃GeTe₂: Boosting the reactivity by the self-reduction of surface hydroxyl, Adv. Funct. Mater. 29 (2019), 1904782.
- [91] A. Zitolo, V. Goellner, V. Armel, M. Sougrati, T. Mineva, L. Stievano, E. Fonda, F. Jaouen, Identification of catalytic sites for oxygen reduction in iron- and nitrogen-doped graphene materials, Nat. Mater. 14 (2015) 937.

- [92] X. Liang, X. Wu, J. Hu, J. Zhao, X.C. Zeng, Large magnetic anisotropy in chemically engineered iridium dimer, Commun. Phys. 1 (2018) 74.
 [93] M. Anand, J.K. Nørskov, Scaling relations in homogeneous catalysis: analyzing the buchwald—hartwig amination reaction, ACS Catal. 10 (2020) 336–345.
- [94] X. Jiang, Q. Liu, J. Xing, N. Liu, Y. Guo, Z. Liu, J. Zhao, Recent progress on 2D magnets: Fundamental mechanism, structural design and modification, Appl. Phys. Rev. 8 (2021), 031305.